Saddle-like, π–conjugated, cyclooctatetrathiophene-based, hole-transporting material for perovskite solar cells

Javier Urieta-Mora,‡[a,b] Inés García-Benito‡[c] Iwan Zimmermann,[c] Juan Aragó,[d] Joaquín Calbo,[d] Giulia Grancini,[c] Agustín Molina-Ontoria,[b] Enrique Ortí,[d]* Nazario Martín,[a,b]* Mohammad Khaja Nazeeruddin[c]**

[a] *Departamento Química Orgánica, Facultad C. C. Químicas, Universidad Complutense de Madrid, Av. Complutense s/n, 28040 Madrid (Spain), Homepage: http://www.ucm.es/info/fullerene/. E-mail: nazmar@ucm.es*

[b] *IMDEA-Nanociencia, C/ Faraday 9, Ciudad Universitaria de Cantoblanco, 28049 Madrid, Spain. E-mail: Agustin.molina@imdea.org*

[c] *Group for Molecular Engineering of Functional Materials and Laboratory for Photonics and Interfaces EPFL VALAIS, CH-1951 Sion, Switzerland. E-mail: mdkhaja.nazeeruddin@epfl.ch.*

[d] *Instituto de Ciencia Molecular, Universidad de Valencia, Catedrático José Beltrán 2, 46980 Paterna, Spain, E-mail: enrique.orti@uv.es*

‡ These authors have contributed equally to the work.

Abstract

A flexible, saddle-like, π-conjugated skeleton containing four fused thiophene rings forming a cyclooctatetrathiophene (CoTh), endowed with four triphenylamines (**CoTh-TTPA**), is presented as hole-transporting material (HTM) for perovskite solar cells. The new HTM shows bright red color stemming from the direct conjugation between the TPA groups and the central CoTh scaffold, resulting in a charge transfer band due to the combination of a slightly acceptor moiety, the CoTh unit, and the electron-donor *p*-methoxytriphenylamine groups. **CoTh-TTPA** exhibits a suitable highest-occupied molecular orbital (HOMO) level regarding the valence band edge of the perovskite, which ensures efficient hole extraction at the perovskite/HTM interface. It has been tested as HTM in combination with a mixed perovskite ($[FAPbI_3]_{0.85}[MAPbBr_3]_{0.15}$) and a state-of-the-art triple cation perovskite ($[(FAPbI_3)_{0.87}(MAPbBr_3)_{0.13}]_{0.92}[CsPbI_3]_{0.08}$) reaching noticeable light-to-energy efficiencies of 16.3 and 15.9 %, respectively, which are slightly lower than those measured for the benchmark spiro-OMeTAD HTM. These values have been analyzed by means of photoluminescence and conductivity experiments, which demonstrated a better hole extraction and conductivity for spiro-OMeTAD.

Introduction

The increasing energy demand and the progressively reduction of the fossil fuels, along with its worrisome effects in our environment, have driven the society in seeking alternatives for the production of energy. The "practically limitless" energy stemming from our Sun represents the most realistic attainable alternative through the optimization of photovoltaic technologies for the transformation of solar energy into electricity. In this regard, perovskites have stepped into the spotlight of the light-harvesting applications due to their outstanding optoelectronic properties, low exciton binding energy, absorption in the whole visible region, tunable band-gap and large exciton diffusion lengths.[1-3] In the first pioneering report, organic–inorganic metal halide perovskites were employed by Miyasaka as light sensitizer for liquid-based, dye-sensitized solar cells (DSSCs) with power conversion efficiencies (PCEs) lower than 3.8 %.[4] Since then, a large variety of mixed perovskites with general ABX_3 formula has been studied. Typically, small organic cations such as methylammonium (MA), formamidinium (FA) or guanidinium (Gua) with a metal dication (Pb^{2+}, Sn^{2+}) and halides as anions (generally Br^- or I^-) are used.[5, 6] Mixing the different components, cations and/or anions, in the perovskite structure leads to the formation of compositionally engineered mixed-perovskites (e. g., $[FAPbI_3]_{1-x}[MAPbBr_3]_x$) that display enhanced properties in comparison with the standard perovskite $MAPbI_3$. By increasing the $MAPbBr_3$ content, blue-shifted absorption of the perovskite material and improvement of the stability is observed.[7]

Owing to the ambipolar charge transport ability of perovskites, alternative device architectures have been explored, either in conventional or in inverted configurations, just varying the charge selective contact. The conventional architecture (n-i-p) can be divided in mesoscopic, using a dense mesoporous layer of TiO_2 (mp-TiO_2), in which the perovskite material is infiltrated into the scaffold, and planar heterojunction, in which the perovskite is sandwiched between an electron-transporting layer (ETL) and a hole-transporting material (HTM).

To date, the best-performing device reported for PSCs incorporates a fluorene-terminated spirobifluorene as HTM in mesoporous structure, reaching PCE values up to 23.2 %.[8, 9] Note that

HTM-free PSC devices only reached limited PCEs (up to 13 %),[10] highlighting the crucial role that HTMs play in the photovoltaic device; not only extracting the photogenerated holes formed within the perovskite film, but also transporting them to the electrodes. Although HTM-based devices exhibit currently a promising stability surpassing one year, improving their stability is an important task to meet the market requirements.

A wide number of HTMs,[11] from polymers[12-14] to inorganic materials,[15-17] have been reported in the literature. Small organic molecules[11] have also received a great attention and, particularly, the well-known and widely used spiro-OMeTAD (2,2′,7,7′-tetrakis(*N*,*N*-di-*p*-methoxyphenylamine)-9,9′-spirobifluorene).[18, 19] The preparation of spiro-OMeTAD requires low temperature and harsh acid/basic conditions along with a sublimation-grade purity to obtain highly efficient devices. These drawbacks have motivated the scientific community to prepare new organic HTMs to develop easily attainable and low-cost materials for large-scale photovoltaic applications. However, a clear relationship between the organic structure of the HTM and the photovoltaic performance has not yet been established. Thus, a vast variety of alternative building blocks has been explored as central scaffolds aiming to outperform the efficiencies attained with spiro-OMeTAD. For instance, spiro-based central scaffolds inspired in spiro-OMeTAD have been extensively studied, providing PCEs over 20 %.[20-22] In addition to the spiro-like HTMs, a wide variety of planar conjugated central cores has been investigated to enhance the hole-carrier mobility of the HTM.[23, 24] π-Extended, sulfur-rich compounds have been used as central scaffolds for constructing new HTMs to favour strong intermolecular π–π interactions.[25-31] Furthermore, donor-acceptor systems following a similar design to that employed for dyes in DSSCs have also been included as potential HTM candidates.[32-34] Additionally, extraordinary simple molecules such as carbazole-based enamine have been reported as HTMs, which achieved excellent photovoltaic performances proving that high structural complexity is not necessary to reach high efficiencies.[35, 36]

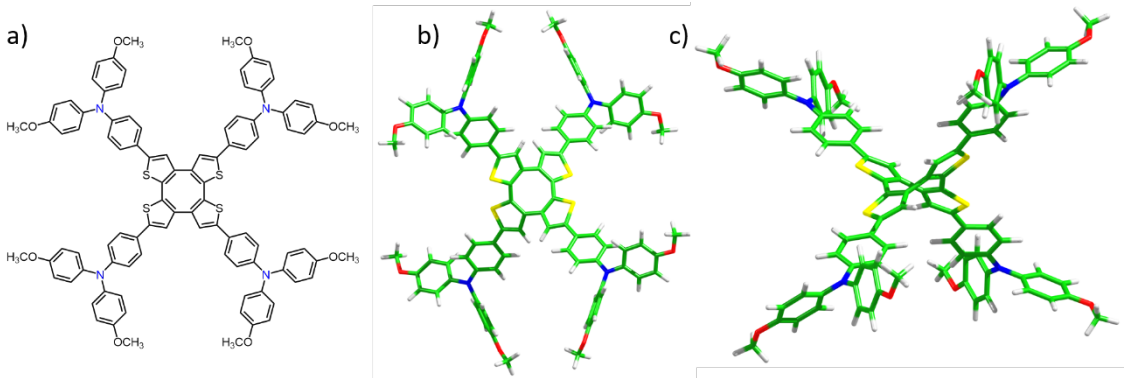

Fig. 1 a) Chemical formula of **CoTh-TTPA**. b) and c) Top and side views of the geometric structure of **CoTh-TTPA** calculated at the B3LYP/6-31G** level in CH_2Cl_2.

Herein, we report a new hole-transporting material (**CoTh-TTPA**) that incorporates an *exotic*, non-planar, 8π, thiophene-rich core, endowed with four *p*-methoxytriphenylamine (TPA) units (Fig. 1). The cyclooctatetrathiophene (CoTh) core is formed by four thiophene rings connected by positions 2 and 3, resulting in a special flexible π-conjugated skeleton with an 8π-electrons annulene core. The non-planar structure of this scaffold could be in principle transformed into a planar geometry by an aromaticity conversion for the reduced 10π dianion or the oxidized 6π dication according to Hückel's $(4n + 2)$ rule. The novel **CoTh-TTPA** HTM has been implemented in mesoporous PSCs in combination with the compositionally engineered perovskite $[FAPbI_3]_{0.85}[MAPbBr_3]_{0.15}$ and also with the triple cation perovskite $[(FAPbI_3)_{0.87}(MAPbBr_3)_{0.13}]_{0.92}[CsPbI_3]_{0.08}$ and the photovoltaic performance of the resulting solar cells has been evaluated. The new HTM exhibits notable efficiencies compared to those reported for the state-of-the-art spiro-OMeTAD. Likewise, a detailed study of the optical, electrochemical and thermal properties of **CoTh-TTPA**, assisted by density functional density (DFT) calculations, is also provided.

Results and discussion

Synthesis of CoTh-TTPA

The synthetic outline for the preparation of the **CoTh-TTPA** HTM is described in Scheme 1. 3,3'-Dibromo-5,5'-bis(trimethylsilyl)-2,2'-bithiophene (**1**) was treated in presence of *n*-BuLi and copper chloride to form the central CoTh motif (**2**) accordingly to a modified synthetic approach

previously reported by Wang.[37-39] Then, selective bromination using N-bromosuccinimide (NBS) followed by a four-fold Suzuki cross-coupling reaction, with the electron-donating *p*-methoxytriphenylamine, successfully afforded the new HTM in a three-step protocol with a good overall yield (44%). Complete structural characterization of **CoTh-TTPA** was achieved using standard techniques such as ^{1}H NMR, ^{13}C NMR, FTIR and mass spectrometry (MALDI-TOF) that confirmed the presence of the aforementioned compound (see the ESI† for further details). As representative spectroscopic features, the ^{1}H NMR spectrum reveals the symmetry of the structure, which exhibits only one singlet (δ = 7.38 ppm) corresponding to the four β protons of the thiophene rings. The chemical structure of **CoTh-TTPA** was ascertained by high-resolution mass spectrometry (HR-MS).

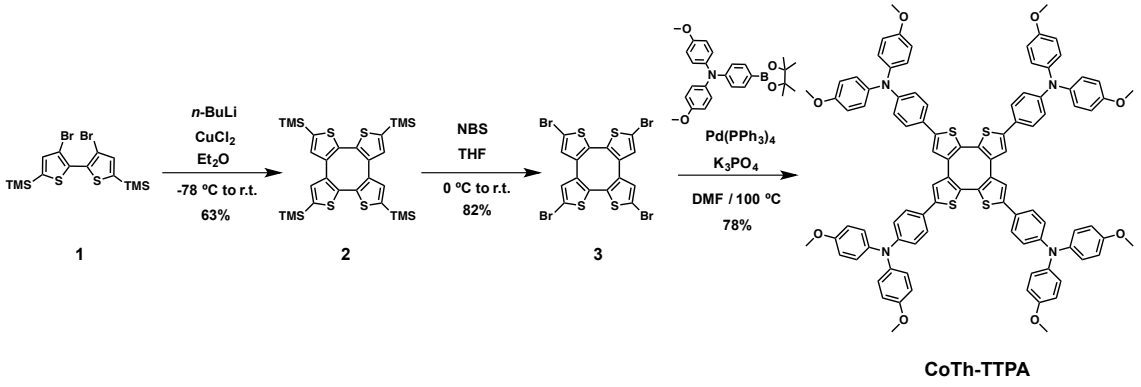

Scheme 1. Synthetic pathway for the preparation of **CoTh-TTPA**

Structural and electronic properties

The structural and electronic properties of the **CoTh-TTPA** HTM were initially studied by performing density functional theory (DFT) calculations at the B3LYP/6-31G** level in the presence of the solvent (CH_2Cl_2). The CoTh core, the pendant triaphenylamine TPA moiety, and the reference spiro-OMeTAD compound were also computed for comparison purposes (see the ESI† for full computational details).

Fig. S1† shows the minimum-energy B3LYP/6-31G**-optimized structures calculated for the CoTh core and the **CoTh-TTPA** HTM, and Fig. S2† displays the most representative bond lengths computed for both systems. The molecular structure is entirely determined by the central cyclooctatetrathiophene unit, which shows a C_2-symmetry saddle-like structure with two opposite

thiophene rings pointing up and the other two pointing down (Fig. 1c and S1†). The distortion from planarity of the central CoTh moiety is characterized by the folding angle α defining the tilting of the thiophene rings with respect to the central molecular plane (Fig. S1†), which has a similar value for both the CoTh core (40º) and the **CoTh-TTPA** HTM (39º). The saddle-like structure obtained for **CoTh-TTPA** is similar to that found for other neutral cyclooctatetraene derivatives.[40] The thiophene rings condensed to the cyclooctatetraene moiety preserve their characteristic structural pattern with a clear single–double carbon–carbon (CC) alternating backbone similar to that found for other related thiophene derivatives.[41, 42] Nevertheless, the inter-thiophene CC bonds are computed to exhibit longer values (1.459 and 1.476 Å) than those obtained, for instance, for linear oligothiophenes (*ca*., 1.420 Å). This lengthening is due to the non-bonding interactions between vicinal thiophene rings and indicates a less effective π-conjugated pathway between these rings. For **CoTh-TTPA**, the insertion of the four TPA units hardly causes any substantial change in the structural shape and in the bond distances of the conjugated core. Regarding the latter, a slight lengthening of the single CC and carbon–sulfur bonds and a shortening of the double CC bonds of the thiophene rings is predicted (Fig. S2†).

Fig. 2 displays the frontier molecular orbitals calculated for TPA, the CoTh core, the **CoTh-TTPA** HTM and the spiro-OMeTAD reference compound. The highest-occupied molecular orbital (HOMO) of the CoTh core, computed at –5.64 eV, is noticeably lower in energy than the HOMO of TPA (–4.77 eV) indicating a weaker electron-donor character. Therefore, for the four-armed **CoTh-TTPA** HTM, the incorporation of the TPA moieties results in a destabilization of the HOMO level (–4.62 eV), improving its electron-donor character and approaching the HOMO level calculated for spiro-OMeTAD (–4.44 eV). Note that the HOMO of **CoTh-TTPA** spreads not only over the central CoTh core but also over the peripheral TPA moieties connected to the thiophene rings. It is important to remark that an important charge transfer occurs from the terminal TPA groups to the sulfur-rich central core, which hold a total net charge of –0.51e for **CoTh-TTPA**. The electronic structure of the **CoTh-TTPA** HTM is therefore predicted to be significantly polarized.

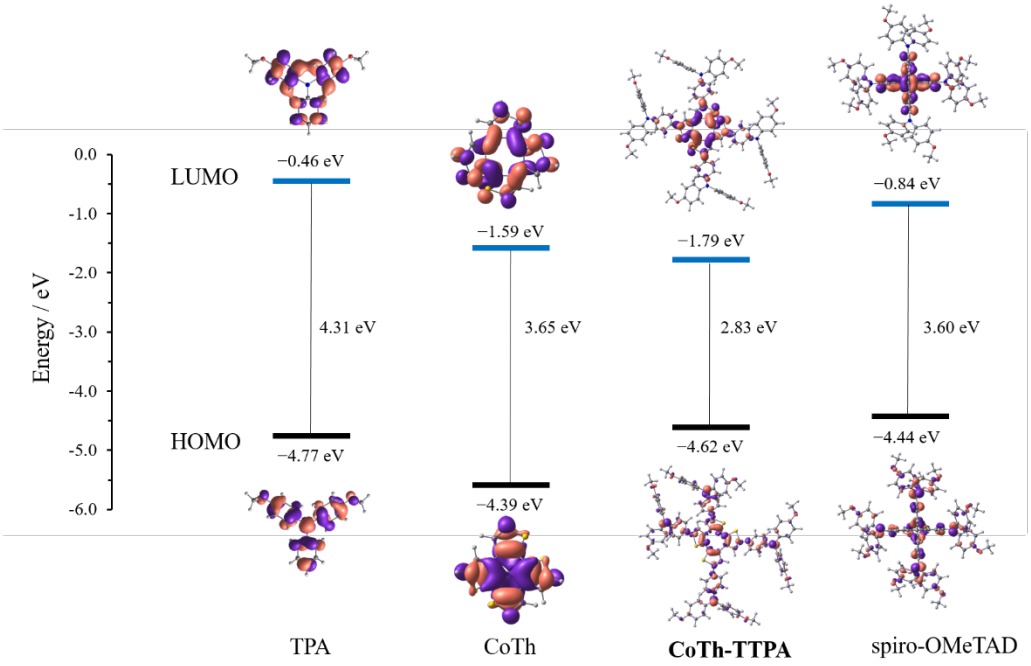

Fig. 2 Energy diagram displaying the frontier molecular orbitals computed at the B3LYP/6-31G** level in CH_2Cl_2 for the TPA unit, the CoTh core, the **CoTh-TTPA** HTM and the spiro-OMeTAD reference compound.

Optical properties

The UV-vis absorption and fluorescence emission spectra of **CoTh-TTPA** registered in dichloromethane solution are shown in Fig. 3a, and the recorded maximum absorption and emission wavelengths are gathered in Table 1. The optical band gap ($E_{0\text{-}0}$) was estimated from the intersection of the absorption and emission bands. In the UV-vis absorption spectrum, two broad absorption bands covering the 250–500 nm range are observed. The first band at shorter wavelengths, peaking at *ca.* 290 nm, is tentatively assigned to the characteristic optical features of the peripheral TPA units, whereas the broad absorption band spreading over the 350–500 nm range is attributed to the π-extension of the central scaffold by introducing the electron-donating TPA units. For **CoTh-TTPA**, it is reasonable to expect the appearance of charge-transfer bands stemming from the direct conjugation between the TPA groups, acting as donor units, and the central CoTh scaffold, acting as the acceptor moiety. This interaction could explain the broad shoulder observed in the absorption located around 400 nm. On the other hand, the emission

spectrum of **CoTh-TTPA** shows a broad fluorescence band peaking at 550 nm with a large Stokes' shift. An optical band gap ($E_{0\text{-}0}$) of 2.70 eV was estimated for **CoTh-TTPA** from the intersection of the absorption and emission bands, which is significantly lower than that recorded for spiro-OMeTAD (3.05 eV) and is in agreement with the narrower HOMO−LUMO gap calculated for **CoTh-TTPA** (Fig. 2).

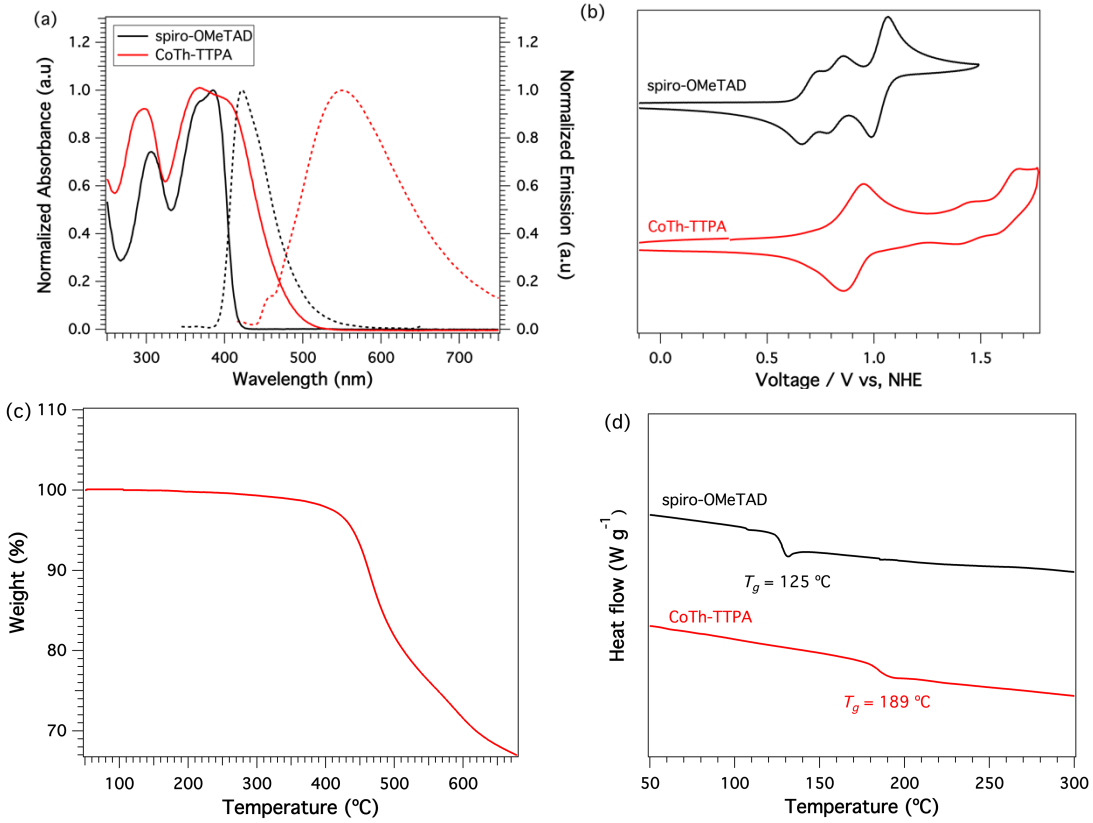

Fig. 3 a) UV-vis absorption spectra (solid line) and fluorescence emission spectra (dashed line) of **CoTh-TTPA** and spiro-OMeTAD recorded in CH_2Cl_2. b) Cyclic voltammetry of **CoTh-TTPA** and spiro-OMeTAD in CH_2Cl_2 containing 0.1 M tetrabutylammonium hexafluorophosphate ($TBAPF_6$) at a scan rate of 100 mV s^{-1}. c) Thermogravimetric analysis curve recorded for **CoTh-TTPA** under nitrogen at 10 °C min^{-1} of heating rate. d) Differential scanning calorimetry curves of **CoTh-TTPA** and spiro-OMeTAD under nitrogen at a heating rate of 20 °C min^{-1} (second cycle).

Table 1. Optical, electrochemical and thermal properties of **CoTh-TTPA** and spiro-OMeTAD.

HTM	$\lambda_{max,\ abs}$ [nm][a]	$\lambda_{max,\ em}$ [nm][a]	$E^{0\text{-}0}$ [eV][b]	$E^{ox}_{1/2}$ [V][c]	E_{HOMO} [eV][d]	E_{LUMO} [eV][e]	T_{dec} [°C][f]	T_g [°C][g]
CoTh-TTPA	396	548	2.70	0.91	–5.35	–2.61	438	189

spiro-OMeTAD	386	419	3.05	0.72	–5.16	–2.11	449	125

[a] λ_{max} of absorption and emission measured in CH_2Cl_2 solutions. [b] $E^{0\text{-}0}$ was determined at the intersection of normalized absorption and emission spectra. [c] Determined from CV measurements *vs* normal hydrogen electrode (NHE). [d] E_{HOMO} is calculated in eV by $E_{HOMO} = –4.44$ eV $– E^{ox}{}_{1/2}$. [e] E_{LUMO} were estimated by $E_{LUMO} = E_{HOMO} + E^{0\text{-}0}$. [f] Decomposition temperature determined from TGA (5% weight loss under a N_2 atmosphere). [g] Determined from the second cycle of the DSC under a N_2 atmosphere.

A theoretical simulation of the absorption spectrum for **CoTh-TTPA** (Fig. S3†) was performed from the B3LYP/6-31G** time-dependent DFT (TDDFT) calculation of the lowest-energy 80 singlet excited electronic states (S_n) in the presence of CH_2Cl_2. The theoretical spectrum correctly reproduces the shape of the experimental spectrum with two intense bands approximately centred at 302 and 430 nm. The lowest-energy band at 430 nm results from the $S_0 \rightarrow S_n$ (n = 1–3 and 5–7) electronic transitions calculated between 521 and 389 nm (Table S1† and Fig. S3†), and gives rise to the experimental broad band centred around 400 nm. These electronic transitions mainly involve one-electron promotions from the HOMO−2, HOMO−1 and HOMO to the LUMO and LUMO+1. They are of π→π* nature, and imply both the excitation of the CoTh core and the charge transfer from the peripheral TPA units to the central CoTh moiety (Table S1† and Fig. S4†). The highest-energy band predicted at 302 nm is associated to the narrower experimental band at 290 nm and shows a complex multiconfigurational nature with predominance of the $S_0 \rightarrow S_{36}$ and S_{38} electronic transitions (Fig. S3†).

Electrochemical properties and reorganization energies

The electrochemical properties of **CoTh-TTPA** were evaluated by cyclic voltammetry (CV) in $TBAPF_6/CH_2Cl_2$ solution at room temperature, at a scan rate of 100 mV s^{-1}, as illustrated in Fig. 3b. The corresponding redox potentials of **CoTh-TTPA** are listed in Table 1. In good accord with the theoretical MO energies discussed above (Fig. 2), **CoTh-TTPA** shows a weaker donor ability, in comparison to spiro-OMeTAD, with a reversible oxidation wave at a half-wave potential ($E_{1/2}$) of 0.91 V *vs* normal hydrogen electrode (NHE). Hence, the HOMO energy level of **CoTh-TTPA** can be estimated around –5.35 eV, while the HOMO energy of the spiro-OMeTAD is upshifted to –5.16 eV. The energy difference of 0.19 eV is in perfect agreement with that predicted

theoretically (0.18 eV, Fig. 2). Therefore, the **CoTh-TTPA** HTM possesses suitable band alignment with the valence band edge of the perovskite (*ca*. −5.65 eV), which may lead to efficient injection of the photogenerated holes from the perovskite to the HTM.

To gain a better understanding of the oxidation processes, the oxidized species (up to the tetracation) of **CoTh-TTPA** were calculated at the B3LYP/6-31G** level in CH_2Cl_2. Table S2† gathers the charges accumulated by the constituting fragments (central core and TPA units) as oxidation takes place. In line with the topology of the HOMO (Fig. 2), the charge for the radical cation species is drawn from the core (*ca.* 0.28e) and the TPA units (0.18e from each unit). Upon further oxidation (dication, trication and tetracations), the charge is steadily extracted from the four TPA units. They hold a similar charge of *ca.* +1.0e for the tetracation and the core loses the excess of electron density found in the neutral state (Table S2†). It should be stressed that for **CoTh-TTPA** the ionization energies (IEs) required for going from the neutral molecule to the cation (IE1), from the cation to the dication (IE2), from the dication to the trication (IE3) and from the trication to the tetracation (IE4) are computed to have comparatively close values (4.51, 4.76, 5.01 and 5.05 eV, respectively), the largest difference being found between IE1 and IE2 (0.25 eV). The closeness of the IEs explains the electrochemical behavior found for **CoTh-TTPA** exhibiting a broad four-electron oxidation wave (Fig. 3b).

To evaluate the capability of the **CoTh-TTPA** system as HTM, hole reorganization energies (λ) were estimated at the B3LYP/6-31G** level in gas phase (see the ESI† for full computational details). The λ value calculated for **CoTh-TTPA** is 0.188 eV, which is notably smaller than the values obtained for its constituting fragments (0.468 and 0.274 eV for CoTh and TPA, respectively). The decrease in λ results from to the fact that charge extraction involves both the core and the terminal TPA moieties. Although **CoTh-TTPA** exhibits a low reorganization energy, the predicted value is larger than that computed for spiro-OMeTAD (0.139 eV).[28]This may be one of the reasons behind why **CoTh-TTPA** shows lower PCE values when used as HTM in PSCs, compared to the archetype spiro-OMeTAD (*vide infra*), despite it presents an appropriate energy level alignment with the valence band edge of the perovskite.

Thermal properties

To ascertain the thermal properties of **CoTh-TTPA**, thermogravimetric analysis (TGA) and differential scanning calorimetry (DSC) were performed (Fig. 3c-d). **CoTh-TTPA** exhibits good thermal stability and decomposes above 400 °C. The morphological stability of the amorphous HTM film upon heating is determined by the glass transition temperature (T_g). DSC provides further evidences of the thermal behaviour of **CoTh-TTPA**. After consecutive heating/cooling cycles, only a T_g value of 186 °C was observed, which confirms the amorphous nature and reduced tendency to crystallize of **CoTh-TTPA**. In contrast, spiro-OMeTAD can exist in both crystalline and amorphous states, with a T_g of 125 °C.

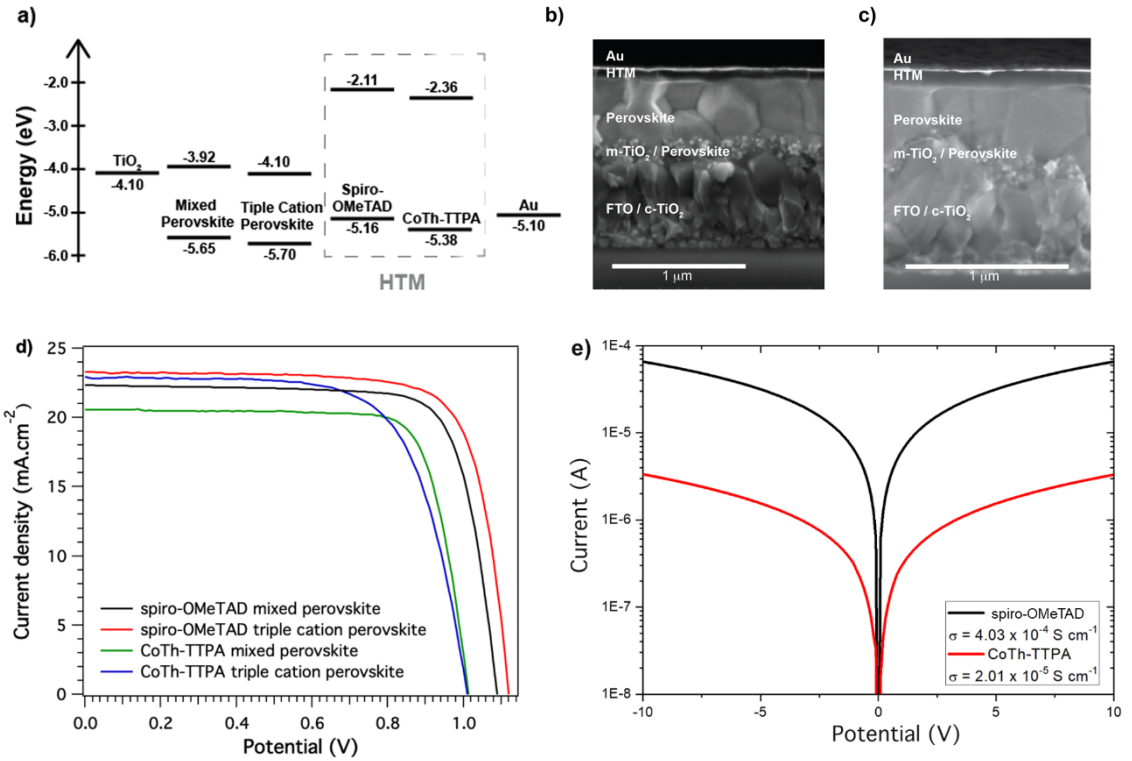

Fig. 4 a) Energy diagram of the different components used in the different PSCs. b) SEM cross-section image of a PSC having **CoTh-TTPA** as HTM and $[FAPbI_3]_{0.85}[MAPbBr_3]_{0.15}$. c) SEM cross-section image of a PSC having **CoTh-TTPA** as HTM and $[(FAPbI_3)_{0.87}(MAPbBr_3)_{0.13}]_{0.92}[CsPbI_3]_{0.08}$. d) Current density–voltage (J–V) curves of **CoTh-TTPA** and spiro-OMeTAD in mesoscopic $[FAPbI_3]_{0.85}[MAPbBr_3]_{0.15}$ and $[(FAPbI_3)_{0.87}(MAPbBr_3)_{0.13}]_{0.92}[CsPbI_3]_{0.08}$-based devices. e) Conductivity of **CoTh-TTPA** and spiro-OMeTAD measured on substrates having interdigitated gold electrodes with a channel length of 2.5 mm.

Photovoltaic characterization

The new small-molecule **CoTh-TTPA** was tested as HTM in mesoscopic solution-processed PSC devices. The energy-level diagram of **CoTh-TTPA** is depicted in Fig. 4a, showing the reasonably matching between the HOMO energy and the valence band edge of the mixed cation-mixed anion perovskite and also with the triple cation perovskite. This provides sufficient driving force for an efficient hole-extraction from the perovskite to the HTM. The different layers constituting the PSC device can be seen from the schematic illustration and the cross-section scanning electron microscopy (SEM) image displayed in Fig. 4b-c. Devices were fabricated from a stack of thin films onto fluorine-doped tin oxide (FTO) conductive glass with the following device configuration FTO/c-TiO_2 (30 nm)/ mp-TiO_2 (200 nm)/ $[FAPbI_3]_{0.85}[MAPbBr_3]_{0.15}$ (600 nm) or $[(FAPbI_3)_{0.87}(MAPbBr_3)_{0.13}]_{0.92}[CsPbI_3]_{0.08}$/HTM/Au (80 nm) as described in detail in the ESI†. The current density-voltage ($J-V$) characteristics obtained from the best-performing device are illustrated in Fig. 4d under 1 sun AM 1.5 G (100 mW cm^{-2}) simulated sunlight, and the corresponding photovoltaic parameters are gathered in Table 2. $[FAPbI_3]_{0.85}[MAPbBr_3]_{0.15}$-based devices employing doped **CoTh-TTPA** afford a maximum PCE of 16.3 % with a short-circuit current (J_{sc}) of 20.6 mA cm^{-2}, a field factor (FF) of 78.3 % and an open-circuit voltage (V_{oc}) of 1.01 V with little hysteresis (Fig. S6†). As a reference, doped spiro-OMeTAD-based PSCs reach a PCE of 18.8 % with a J_{sc} of 22.35 mA cm^{-2}, a FF of 77.3 and a V_{oc} of 1.09 V with little hysteresis (Fig. S7†). The performance of the spiro-OMeTAD can be significantly increased by changing the perovskite to $[(FAPbI_3)_{0.87}(MAPbBr_3)_{0.13}]_{0.92}[CsPbI_3]_{0.08}$. The champion-device displays a PCE of 19.94 % with a J_{sc} of 23.3 mA cm^{-2}, a FF of 76.5 % and a V_{oc} of 1.12 V with little hysteresis (Fig. S8†). Conversely, **CoTh-TTPA**-based devices with $[(FAPbI_3)_{0.87}(MAPbBr_3)_{0.13}]_{0.92}[CsPbI_3]_{0.08}$ exhibit lower efficiency than those using the mixed cation-mixed anion perovskite. The devices afford a maximum PCE of 15.88 % with a J_{sc} of 22.3 mA cm^{-2}, a FF of 68.5 % and a V_{oc} of 1.01 V, with noticeable hysteresis (Fig. S9†). The small difference in the performances is probably due to the homogeneity of the HTM film deposited on top of the perovskite layer, and the hysteresis can be due to accumulation of charges at the perovskite/HTM interface. The SEM

images of the surface show that the HTM thin film was indeed more uniform and smoother when employing the double-cation perovskite, than when deposited onto the triple-cation perovskite (Fig. S10†). This results in a significant difference in the FF, which is higher in the case of the double cation-based perovskite and leads to a better PCE using this perovskite. The integrated current densities from the external quantum efficiencies (EQEs) are in good agreement, within 5%, with those obtained from the $J-V$ measurements (Fig. S11 and S12†).

To gain more insight into the charge extraction processes at the perovskite/HTM interface, steady-state photoluminescence (PL) was recorded (Fig. S14†). The pristine perovskite film shows a strong PL signal which stems from the radiative recombination of the photogenerated charge carriers. After deposition of the HTM on top of the perovskite, the intensity of the PL signal is significantly reduced. This quenching is caused by the efficient extraction of the photogenerated charge carriers, and is remarkably enhanced for the perovskite/spiro-OMeTAD. Compared to spiro-OMeTAD, **CoTh-TTPA** exhibits a smaller quenching, which suggests a less efficient hole extraction from the perovskite that is significantly improved for the triple cation perovskite (Fig. S14†). The lower hole extraction ability of **CoTh-TTPA** is ascribed to its poorer electron-donor character, compared to spiro-OMeTAD, which is related to the saddle-like structure of **CoTh-TTPA** that breaks the π-conjugation across the polycyclic core.

Table 2. Device performance of **CoTh-TTPA** HTM with $[FAPbI_3]_{0.85}[MAPbBr_3]_{0.15}$ and $[(FAPbI_3)_{0.87}(MAPbBr_3)_{0.13}]_{0.92}[CsPbI_3]_{0.08}$ perovskites and compared with the reference spiro-OMeTAD.

HTM	Perovskite	V_{oc} (mV)	J_{sc} (mA cm^{-2})	FF (%)	PCE (%)
CoTh-TTPA	$[FAPbI_3]_{0.85}[MAPbBr_3]_{0.15}$	1013	20.56	78.3	16.30
CoTh-TTPA	$[(FAPbI_3)_{0.87}(MAPbBr_3)_{0.13}]_{0.92}[CsPbI_3]_{0.08}$	1010	22.95	68.5	15.88
spiro-OMeTAD	$[FAPbI_3]_{0.85}[MAPbBr_3]_{0.15}$	1090	22.35	77.3	18.8
spiro-OMeTAD	$[(FAPbI_3)_{0.87}(MAPbBr_3)_{0.13}]_{0.92}[CsPbI_3]_{0.08}$	1120	23.29	76.5	19.94

To further investigate the lower efficiency observed for **CoTh-TTPA**, we measured the conductivity of the HTM on organic field-effect transistor (OFET) substrates (Fig. 4e). Same concentration as for the device preparation was used adding 6% of FK-209 as dopant for both **CoTh-TTPA** and spiro-OMeTAD. The conductivity of spiro-OMeTAD ($4.03 \times \cdot 10^{-4}$ S·cm^{-1}) is one order of magnitude higher than the conductivity of **COTh-TTPA** ($2.0.1 \cdot \times 10^{-5}$ S·cm^{-1}), which further confirms the lower efficiency of the latter.

Conclusions

In summary, we have designed, synthesized and characterized a new saddle-like hole-transporting material based on a cyclooctatetrathiophene central core which is further endowed with *p*-methoxytriphenylamines (**CoTh-TTPA**). **CoTh-TTPA** exhibits a much deeper HOMO energy level along with a higher glass transition temperature than the state-of-the-art spiro-OMeTAD. The quenching of the photogenerated charge carrier occurred more efficiently at the interface between the spiro-OMeTAD and the perovskite when compared to **CoTh-TTPA**/perovskite interface. Furthermore, thin-film transistors based on spiro-OMeTAD show one order of magnitude higher in conductivity than the respective device based on **CoTh-TTPA**. The novel compound was employed as HTM in PSCs using two different perovskites, $[FAPbI_3]_{0.85}[MAPbBr_3]_{0.15}$ and the state-of-the-art triple cation $[(FAPbI_3)_{0.87}(MAPbBr_3)_{0.13}]_{0.92}[CsPbI_3]_{0.08}$ perovskite. Energy conversion efficiencies of up to 16.3 % were obtained for **CoTh-TTPA**, which are lower than those for the spiro-OMeTAD. The lower performance of **CoTh-TTPA** is ascribed to its higher reorganization energy, lower conductivity along with its poorer hole extraction ability.

Conflicts of interest

There are no conflicts to declare.

Acknowledgments

We thank the Swiss National Funds for Scientific Research contract number 200020L_172929/1, Project "Tailored Design and in-depth understanding of perovskite solar materials using in-house developed 3D/4D nanoscale ion-beam analysis". Borun New Material Technology generously supplied the high-quality spiro-OMeTAD. The authors also thank the European Research Council (ERC-320441-Chirallcarbon), the Spanish Ministry of Economy and Competitiveness MINECO (projects CTQ2017-83531-R, CTQ2015-71154-P, CTQ2016-81911-REDT, Centro de Excelencia Severo Ochoa SEV-2016-0686 and Unidad de Excelencia María de Maeztu MDM-2015-0538), CAM (FOTOCARBON project S2013/MIT-2841), the Generalitat Valenciana (PROMETEO/2016/135 and SEJI/2018/035) and European Feder funds (CTQ2015-71154-P). J.A. is grateful to MINECO for a "Ramon-y-Cajal" fellowship (RyC-2017-23500). J.C. also acknowledges the Generalitat Valenciana for a Vali+d post-doctoral fellowship (APOSTD/2017/081). I.G.B and G.G. acknowledge the Swiss National Science Foundation (SNSF) funding through the Ambizione Energy project Hyper (Grand number PZENP2_173641).

Notes and references

1. M. M. Lee, J. Teuscher, T. Miyasaka, T. N. Murakami and H. J. Snaith, *Science*, 2012, **338**, 643-647.
2. Y. Zhao and K. Zhu, *Chem. Soc. Rev.*, 2016, **45**, 655-689.
3. T. M. Brenner, D. A. Egger, L. Kronik, G. Hodes and D. Cahen, *Nat. Rev. Mater.*, 2016, **1**, 15007.
4. A. Kojima, K. Teshima, Y. Shirai and T. Miyasaka, *J. Am. Chem. Soc.*, 2009, **131**, 6050-6051.
5. G. E. Eperon, S. D. Stranks, C. Menelaou, M. B. Johnston, L. M. Herz and H. J. Snaith, *Energy Environ. Sci.*, 2014, **7**, 982-988.
6. A. D. Jodlowski, C. Roldán-Carmona, G. Grancini, M. Salado, M. Ralaiarisoa, S. Ahmad, N. Koch, L. Camacho, G. de Miguel and M. K. Nazeeruddin, *Nat. Energy*, 2017, **2**, 972-979.
7. N. J. Jeon, J. H. Noh, W. S. Yang, Y. C. Kim, S. Ryu, J. Seo and S. I. Seok, *Nature*, 2015, **517**, 476-480.
8. N. R. E. L. National Renewable Energy Laboratory, 2018.
9. N. J. Jeon, H. Na, E. H. Jung, T.-Y. Yang, Y. G. Lee, G. Kim, H.-W. Shin, S. Il Seok, J. Lee and J. Seo, *Nat. Energy*, 2018, **3**, 682-689.
10. G. Grancini, C. Roldán-Carmona, I. Zimmermann, E. Mosconi, X. Lee, D. Martineau, S. Narbey, F. Oswald, F. De Angelis, M. Graetzel and M. K. Nazeeruddin, *Nat. Commun.*, 2017, **8**, 15684.
11. J. Urieta-Mora, I. García-Benito, A. Molina-Ontoria and N. Martín, *Chem. Soc. Rev.*, 2018, **47**, 8541-8571.

12. J. H. Heo, S. H. Im, J. H. Noh, T. N. Mandal, C.-S. Lim, J. A. Chang, Y. H. Lee, H.-j. Kim, A. Sarkar, M. K. Nazeeruddin, M. Grätzel and S. I. Seok, *Nat. Photonics*, 2013, **7**, 486.
13. W. S. Yang, B.-W. Park, E. H. Jung, N. J. Jeon, Y. C. Kim, D. U. Lee, S. S. Shin, J. Seo, E. K. Kim, J. H. Noh and S. I. Seok, *Science*, 2017, **356**, 1376.
14. G. W. Kim, J. Lee, G. Kang, T. Kim and T. Park, *Adv. Energy. Mater.*, 2018, **8**, 1870018.
15. H. Zhang, H. Wang, W. Chen and K. Y. Jen Alex, *Adv. Mater.*, 2016, **29**, 1604984.
16. M. Jung, C. Kim Young, J. Jeon Nam, S. Yang Woon, J. Seo, H. Noh Jun and S. Il Seok, *ChemSusChem*, 2016, **9**, 2592-2596.
17. N. Arora, M. I. Dar, A. Hinderhofer, N. Pellet, F. Schreiber, S. M. Zakeeruddin and M. Grätzel, *Science*, 2017.
18. N. J. Jeon, H. G. Lee, Y. C. Kim, J. Seo, J. H. Noh, J. Lee and S. I. Seok, *J. Am. Chem. Soc.*, 2014, **136**, 7837-7840.
19. D. Bi, W. Tress, M. I. Dar, P. Gao, J. Luo, C. Renevier, K. Schenk, A. Abate, F. Giordano, J.-P. Correa Baena, J.-D. Decoppet, S. M. Zakeeruddin, M. K. Nazeeruddin, M. Grätzel and A. Hagfeldt, *Sci. Adv.*, 2016, **2**, e1501170.
20. M. Saliba, S. Orlandi, T. Matsui, S. Aghazada, M. Cavazzini, J.-P. Correa-Baena, P. Gao, R. Scopelliti, E. Mosconi, K.-H. Dahmen, F. De Angelis, A. Abate, A. Hagfeldt, G. Pozzi, M. Graetzel and M. K. Nazeeruddin, *Nat. Energy*, 2016, **1**, 15017.
21. B. Xu, J. Zhang, Y. Hua, P. Liu, L. Wang, C. Ruan, Y. Li, G. Boschloo, E. M. J. Johansson, L. Kloo, A. Hagfeldt, A. K. Y. Jen and L. Sun, *Chem*, **2**, 676-687.
22. Y. Wang, Z. Zhu, C. C. Chueh, K. Y. Jen Alex and Y. Chi, *Adv. Energy. Mater.*, 2017, **7**, 1700823.
23. K. Rakstys, S. Paek, P. Gao, P. Gratia, T. Marszalek, G. Grancini, K. T. Cho, K. Genevicius, V. Jankauskas, W. Pisula and M. K. Nazeeruddin, *J. Mat. Chem. A*, 2017, **5**, 7811-7815.
24. S. Paek, P. Qin, Y. Lee, K. T. Cho, P. Gao, G. Grancini, E. Oveisi, P. Gratia, K. Rakstys, S. A. Al-Muhtaseb, C. Ludwig, J. Ko and M. K. Nazeeruddin, *Adv. Mater.*, 2017, **29**, n/a-n/a.
25. S. Kazim, F. J. Ramos, P. Gao, M. K. Nazeeruddin, M. Grätzel and S. Ahmad, *Energy Environ. Sci.*, 2015, **8**, 1816-1823.
26. R. Azmi, S. Y. Nam, S. Sinaga, Z. A. Akbar, C.-L. Lee, S. C. Yoon, I. H. Jung and S.-Y. Jang, *Nano Energy*, 2018, **44**, 191-198.
27. A. Molina-Ontoria, I. Zimmermann, I. Garcia-Benito, P. Gratia, C. Roldán-Carmona, S. Aghazada, M. Graetzel, M. K. Nazeeruddin and N. Martín, *Angew. Chem. Int. Ed.*, 2016, **55**, 6270-6274.
28. I. Zimmermann, J. Urieta-Mora, P. Gratia, J. Aragó, G. Grancini, A. Molina-Ontoria, E. Ortí, N. Martín and M. K. Nazeeruddin, *Adv. Energy. Mater.*, 2017, **7**, 1601674.
29. I. Garcia-Benito, I. Zimmermann, J. Urieta-Mora, J. Arago, A. Molina-Ontoria, E. Orti, N. Martin and M. K. Nazeeruddin, *J. Mat. Chem. A*, 2017, **5**, 8317-8324.
30. J. Urieta-Mora, I. Zimmermann, J. Aragó, A. Molina-Ontoria, E. Ortí, N. Martín and M. K. Nazeeruddin, *Chem. Mater.*, 2018, DOI: 10.1021/acs.chemmater.8b04003.
31. R. Sandoval-Torrientes, I. Zimmermann, J. Calbo, J. Aragó, J. Santos, E. Ortí, N. Martín and M. K. Nazeeruddin, *J. Mat. Chem. A*, 2018, **6**, 5944-5951.

32. Z. a. Li, Z. Zhu, C.-C. Chueh, S. B. Jo, J. Luo, S.-H. Jang and A. K. Y. Jen, *J. Am. Chem. Soc.*, 2016, **138**, 11833-11839.
33. N. Arora, C. Wetzel, M. I. Dar, A. Mishra, P. Yadav, C. Steck, S. M. Zakeeruddin, P. Bäuerle and M. Grätzel, *ACS Appl. Mater. Interfaces*, 2017, **9**, 44423-44428.
34. X. Sun, Q. Xue, Z. Zhu, Q. Xiao, K. Jiang, H.-L. Yip, H. Yan and Z. a. Li, *Chem. Sci.*, 2018, **9**, 2698-2704.
35. F. Zhang, Z. Wang, H. Zhu, N. Pellet, J. Luo, C. Yi, X. Liu, H. Liu, S. Wang, X. Li, Y. Xiao, S. M. Zakeeruddin, D. Bi and M. Grätzel, *Nano Energy*, 2017, **41**, 469-475.
36. M. Daskeviciene, S. Paek, Z. Wang, T. Malinauskas, G. Jokubauskaite, K. Rakstys, K. T. Cho, A. Magomedov, V. Jankauskas, S. Ahmad, H. J. Snaith, V. Getautis and M. K. Nazeeruddin, *Nano Energy*, 2017, **32**, 551-557.
37. Y. Wang, D. Gao, J. Shi, Y. Kan, J. Song, C. Li and H. Wang, *Tetrahedron*, 2014, **70**, 631-636.
38. C. Zhao, L. Xu, Y. Wang, C. Li and H. Wang, *Chin. J. Chem.*, 2014, **33**, 71-78.
39. Y. Wang, Z. Wang, D. Zhao, Z. Wang, Y. Cheng and H. Wang, *Synlett*, 2007, **2007**, 2390-2394.
40. K. Mouri, S. Saito and S. Yamaguchi, *Angew. Chem. Int. Ed.*, 2012, **51**, 5971-5975.
41. J. Arago, P. M. Viruela, J. Gierschner, E. Orti and B. Milian-Medina, *Phys. Chem. Chem. Phys.*, 2011, **13**, 1457-1465.
42. J. Aragó, R. Ponce Ortiz , B. Nieto-Ortega, V. Hernández, J. Casado, A. Facchetti, T. J. Marks, P. M. Viruela, E. Ortí and J. T. López Navarrete, *ChemPhysChem*, 2012, **13**, 168-176.

TOC

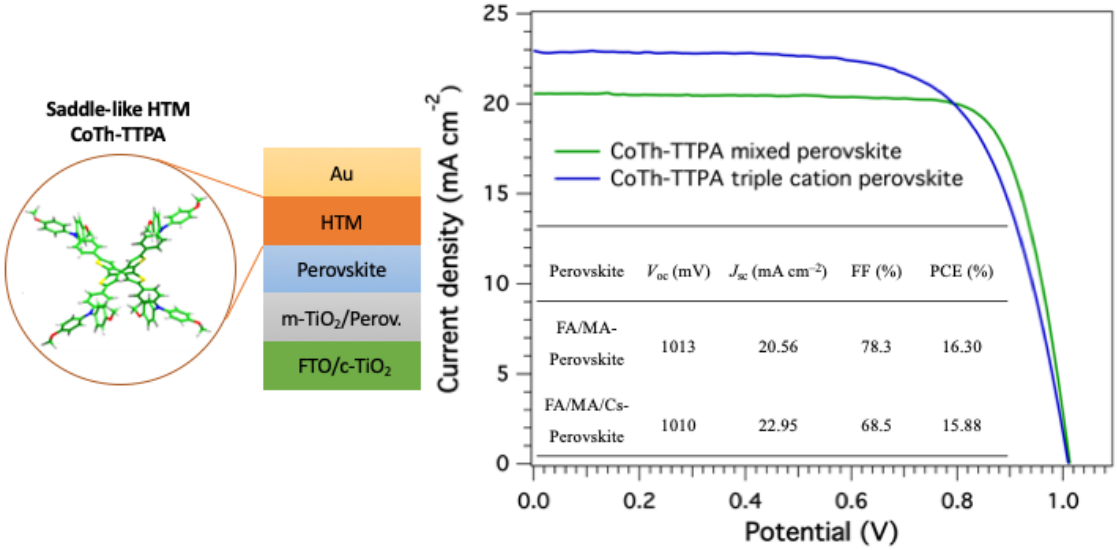

A saddle-like hole-transporting material incorporating a non-planar, thiophene-rich core endowed with four p-methoxytriphenylamine units is presented. The new HTM leads to PSCs reaching efficiencies up to 16.3 %.